IEEE Access
Multidisciplinary | Rapid Review | Open Access Journal

Received April 14, 2020, accepted May 1, 2020, date of publication May 11, 2020, date of current version May 26, 2020.

Digital Object Identifier 10.1109/ACCESS.2020.2993865

Experimental Study of Single-Transmitter-Based Precise Indoor Positioning System

O-JONG KIM[1], DANIEL HONG[1], JUNGBEOM KIM[1], TAIKJIN LEE[2], AND CHANGDON KEE[1]
[1]Department of Aerospace Engineering & IAMD, Seoul National University, Seoul 08826, South Korea
[2]Sensor System Research Center, Korea Institute of Science and Technology, Seoul 02792, South Korea

Corresponding author: Changdon Kee (kee@snu.ac.kr)

This work was supported in part by the Basic Science Research Program through the National Research Foundation of Korea (NRF) funded by the Ministry of Science, ICT & Future Planning, contracted through by the Institute of Advanced Aerospace Technology at Seoul National University under Grant NRF-2017M1A3A3A02016230.

ABSTRACT A single-transmitter-based positioning system using an antenna array has been designed and developed to minimize the number of transmitters needed for environments where satellite-based navigation systems are unavailable. One of its suitable applications is for indoor navigation. The user receives the signals from the antenna array and calculates the position using the carrier-phase measurements. A key feature of the system is that the number of cycle ambiguity candidates is geometrically bounded. If the length of the antenna baseline is smaller than half the wavelength, the ambiguity resolution process is unnecessary. To improve the positioning performance for practical use, the antenna baseline must be enlarged. Even in this case, the cycle ambiguity resolution issue can be resolved fast and accurately. For instance, there are only nine candidates according to the setting of the study. To investigate the performance of the system, experiments for a dynamic rover using multiple ''pseudolites,'' pseudo-satellite transmitters, were conducted. In addition, low-cost inertial measurement unit (IMU) sensors were combined to investigate the improved positioning accuracy. Experimental results showed that positioning root-mean-square errors were 18 cm and 25 cm with IMU and without IMU, respectively, at the scale of a conventional meeting room. All integer-cycle ambiguities were solved accurately during the experiments, and more than 93% were resolved within 5 s.

INDEX TERMS Antenna array, cycle ambiguity resolution, indoor positioning, inertial measurement unit, pseudolite, single-transmitter-based positioning.

I. INTRODUCTION

The focus of this study is the application of a single-transmitter-based positioning system for indoor navigation. These systems have been suggested for non-global navigation satellite system (non-GNSS) environments, such as indoor navigation [1], [2] and alternative position, navigation, and timing systems (APNT) [3]–[8], because of their compactness, cost-effectiveness, and accuracy.

Inside a building or structure, GNSS signals cannot reach users, because of the inherently low intensity of the signals. Therefore, an independent navigation system is essential for indoor applications, and various studies have been conducted to find solutions to meet the increased demand for indoor location-based services [9]–[11]. The single-transmitter-based positioning system using an antenna array, which is termed the ''Mosaic system'' in this paper, has also been studied for indoor applications, considering its special features as follows:

- A single transmitter system can provide a positioning service that minimizes the number of transmitters.
- Standalone positioning is available without needing external information, such as a database or map.
- Continuous positioning is available to keep track of the user's trajectory.
- As it is the user who calculates the position, not the server or other external components, privacy and security are maintained.

In the Mosaic system, the transmitter generates multi-channel signals and broadcasts using an antenna array. In this study, a pseudolite is used as a signal generator. A pseudolite is a transmitter that broadcasts the GNSS signal on the ground; therefore, a conventional GNSS receiver can be utilized to receive the signals [12]. Users calculate their own

The associate editor coordinating the review of this manuscript and approving it for publication was Giorgio Montisci.

positions by utilizing the time difference of arrival (TDOA) of the carrier-phase measurements.

Another feature of this system is carrier-phase measurements whose noise level is very low and is used to overcome the poor dilution-of-precision (DOP) environment, which is unavoidable because only a single transmitter is covering the target field. However, relying on the carrier-phase causes the problem of integer-cycle ambiguity, an unknown integer term multiplied by the wavelength. For the positioning of a carrier-phase based system, the cycle ambiguities must first be fixed. For the Mosaic system, the length of the transmitter's antenna baseline is a key feature to solve the cycle ambiguity problem.

The authors' research group researched the Mosaic system thoroughly. Basic Mosaic was a cycle ambiguity-free system with a limited antenna baseline smaller than half of the wavelength (9.51 cm for a 1575.42 MHz carrier) [1]. Simulation-based analyses for indoor positioning performance of the system, including multipath error modeling, were conducted [13]. Another application was for an APNT service to present the terrestrial-based three-dimensional (3D) positioning for aviation users when GNSS is unavailable because of signal interference [3]. The antenna baseline should be long to cover a wide area, up to a few hundred kilometers. In this case, the process of the cycle ambiguity resolution is essential for positioning. However, the ambiguity can be resolved very fast, unlike in a carrier-phase-based GNSS system, because the number of candidates is geometrically bounded according to the shape of the antenna array. Simulation-based studies for ambiguity resolution have been performed [4], [6], including the strategy of designing the antenna array for both positioning accuracy and fast ambiguity resolution [7], [8]. A study of error sources, such as multipath, tropospheric delay, and antenna misalignment, has also been presented [5].

The studies mentioned above have been conducted based on simulations for conceptual analyses only. Recently, preliminary experiments on two-dimensional (2D) positioning for static users according to the length of the antenna baseline were performed in an indoor environment [14]. Although the preliminary study considered an antenna baseline longer than half of the wavelength to improve the positioning accuracy, the cycle ambiguity problem, essential for a fully functional positioning system, was not considered properly. Instead, it was assumed that the cycle ambiguities were fixed. In addition, the positioning performance only for static users was investigated.

Studies of the single-transmitter-based indoor positioning system using multi-channel pseudolites have also been performed by others [15]. TDOA was also applied for hyperbolic positioning using carrier-phase measurements. The length of the antenna baseline was set to only half of the wavelength to eliminate the process for cycle ambiguity resolution. Experiments for 2D positioning for static users were conducted, and it demonstrated a bias up to the meter level. In addition, simulation-based analyses for 3D positioning were also conducted with convergence investigation. There have been different studies that used multi-channel pseudolite-based antenna arrays for indoor applications [16], [17]. Eight multi-channels were configured for the system, and it achieved high accuracy. However, the initial position of the user was required for positioning.

The first contribution of this paper is that it presents the single-transmitter-based precise indoor positioning system with experimental validation for dynamic users. In previous studies, experimental analyses of positioning accuracy were only conducted for static users [14], [15]. Previous works [13], [15] only considered using the antenna baseline of half of the wavelength. Therefore, the positioning performance is not appropriate for precise positioning. However, in this study, using longer antenna baselines to improve the positioning accuracy is considered with a method to solve the cycle ambiguity problem directly. In addition, smartphone-based, low-cost inertial measurement units (IMUs) are utilized and combined with Kalman filtering to investigate improved positioning accuracy for indoor users. Measurement residuals and DOP analyses are also conducted to describe the special features of the Mosaic system.

The second contribution is that it presents a valid method for the successful fixing of the cycle ambiguity problem without a known initial position in indoor experiments. In general, cycle ambiguities have been fixed by using a known initial position for an indoor pseudolite-based system [16]–[19]. However, for the cycle ambiguity resolution process of the Mosaic system, a residual-based test with the mitigation method utilizing the length of the antenna baseline can be applied for fast and robust ambiguity resolution without knowing the initial position of a dynamic user [4], [6], [8]. This is the first study to obtain the experimental results of fast ambiguity resolution using an antenna array in the indoor environment.

II. MOSAIC SYSTEM

A. SYSTEM CONCEPT

A conceptual design of the Mosaic system is depicted in Fig. 1. A single transmitter with multiple RF parts generates signals for each channel. All channels share one clock source for synchronizing the signals. Signals from each channel should be distinguishable, such as by using different pseudo-random noises (PRNs). If a multi-channel global positioning system (GPS) pseudolite transmitter is utilized for the Mosaic system, it generates the GPS L1 frequency, and Gold code is used for the PRNs.

The user segment, using the receiver with a single antenna, receives signals from each channel and calculates the TDOAs from each antenna, removing the integer-cycle ambiguity of the carrier-phase measurements. Positioning can be performed using the TDOA measurements.

The minimum number of antennas required for 2D positioning is three when the antenna baseline length is smaller than half of the wavelength (0.5 λ) [13]–[15]. If the antenna baseline length is longer than this for better positioning

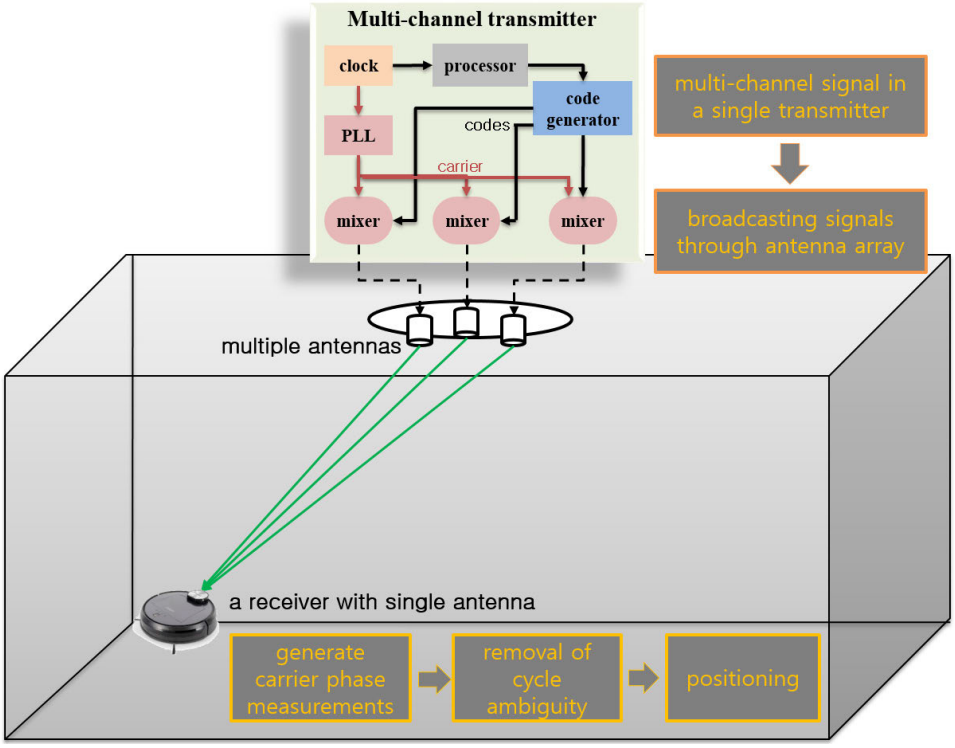

FIGURE 1. Conceptual design of the Mosaic system (three-channel case).

accuracy, the process of cycle ambiguity resolution is generally required. In this case, more antennas are favorable for the performance of cycle ambiguity resolution.

Usable 3D positioning can be achieved if there is an additional height or distance measurement from the transmitter to the user, because the error ellipse of a single-transmitter-based system is extremely large along the radial direction from the transmitter [6].

In this study, GPS L1 pseudolites were used for 2D positioning with the assumption that the height difference between the rover-type user and the transmitting antenna is fixed and unchanged. The antenna baseline length of 1.5 λ was set for better positioning accuracy, because the accuracy of previous studies using the antenna baseline of 0.5 λ was not enough for precise positioning [14], [15]. To improve the cycle ambiguity resolution, five pseudolites and antennas were configured for our investigation.

Although the concept for the Mosaic system considers a time-synchronized multi-channel transmitter, the pseudolite testbed used in this study was not fully synchronized. Instead, a reference receiver was used to eliminate the clock and channel biases of the transmitter. Similar results in this study are expected when a time-synchronized multi-channel pseudolite system is utilized without the use of a reference receiver because a well-designed multi-channel pseudolite system has already been successfully utilized for experiments [15]–[17].

Measurement equations in this section assume that the pseudolite signals are time-synchronized to represent the general approach of the Mosaic system to treat the cycle ambiguity problem. Equations actually used for experiments of this study will be presented in section II.B in detail.

Since TDOA is utilized for positioning, a single-difference carrier-phase (SDCP) measurement is mainly considered. SDCP can be expressed using (1)–(3). Equation (1) expresses the measurement of GNSS signals [20] as follows:

$$\phi^j = d^j + N^j\lambda + B - b + t^j - i^j + m^j + \varepsilon^j, \tag{1}$$

where ϕ is the measured carrier phase in metric, d is the distance between the pseudolite and the user, N is an unknown integer term of cycle ambiguity, λ is the wavelength of the carrier signal, B is the receiver clock offset, b is the transmitter clock offset, t is the tropospheric delay, i is the ionospheric delay, m is the multipath error, ε is other noise, and superscript j represents the measurement from the j-th pseudolite.

Equation (1) can be reduced to (2), which is appropriate for indoor environments, eliminating tropospheric and ionospheric delays:

$$\phi^j = d^j + N^j\lambda + B - b + m^j + \varepsilon^j. \tag{2}$$

For SDCP measurements, (2) can be rewritten using pseudolites 1 and 2 as (3). The receiver clock offset is eliminated because of the difference process. The transmitter clock offset can be disregarded if each pseudolite shares one clock source for time synchronization. ε' is defined as the combination of the multipath error m and noise ε to represent all errors in one notation.

$$\nabla^{12}\phi \equiv \phi^1 - \phi^2$$

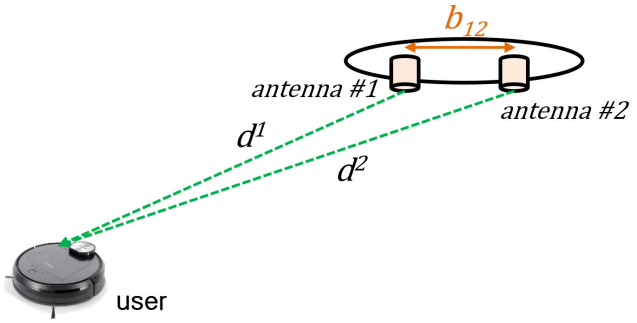

FIGURE 2. Geometric description for two-antenna case.

$$= \nabla^{12}d + \nabla^{12}N\lambda + \nabla^{12}\varepsilon'. \tag{3}$$

Once (3) is divided by wavelength λ and rounded, the integer ambiguity can be described as follows by (4):

$$\nabla^{12}N = \text{round}\left(\frac{\nabla^{12}\phi}{\lambda}\right) - \text{round}\left(\frac{\nabla^{12}d + \nabla^{12}\varepsilon'}{\lambda}\right). \tag{4}$$

In Fig. 2, b_{12} denotes the distance between the first pseudolite antenna and the second antenna and is always greater than $\nabla^{12}d$. b_{12} can always be expressed using a certain integer M and $p(0 \le p < 0.5)$, as shown in (5).

$$b_{12} \le (M + p)\,\lambda \tag{5}$$

If $\nabla^{12}d$ is positive; then, the following is satisfied:

$$\text{round}\left(\frac{\nabla^{12}d + \nabla^{12}\varepsilon'}{\lambda}\right) \le \text{round}\left(\frac{(M+p)\lambda + \nabla^{12}\varepsilon'}{\lambda}\right) = M + \text{round}\left(p + \frac{\nabla^{12}\varepsilon'}{\lambda}\right). \tag{6}$$

The last round term of (6) is required to be set to 0 with an appropriate value of p. If the error term $\nabla^{12}\varepsilon'$ is greater, then p should be made smaller to make the round term 0. M is the minimum integer required to satisfy (5) with the given antenna spacing b_{12}. If (4) and (6) are combined, the lower bound of the cycle ambiguity is as follows:

$$\nabla^{12}N \ge \text{round}\left(\frac{\nabla^{12}\phi}{\lambda}\right) - M. \tag{7}$$

Considering the negative case of $\nabla^{12}d$, the upper and lower bounds are expressed as follows:

$$-M + \text{round}\left(\frac{\nabla^{12}\phi}{\lambda}\right) \le \nabla^{12}N \le M + \text{round}\left(\frac{\nabla^{12}\phi}{\lambda}\right). \tag{8}$$

Equation (8) geometrically bounds the cycle ambiguity between pseudolites 1 and 2. In other words, the existence of the true cycle integer is guaranteed within the geometrical bounds. If the length of the antenna baseline is slightly smaller than 1.5 λ, the number of ambiguity candidates is 3: the candidates of M are -1, 0, and 1 for each SDCP measurement.

B. POSITIONING ALGORITHM

In section II.A, it is assumed that the transmitting signals are time-synchronized with a common clock bias. In this section, the positioning algorithm used for the experimental study is derived with the consideration that the pseudolites are not synchronized, as in (9) from (3):

$$\nabla_u^{12}\phi = \nabla_u^{12}d + \nabla_u^{12}N\lambda - \nabla^{12}b + \nabla_u^{12}\varepsilon', \tag{9}$$

where the subscript u denotes the user receiver.

The reference receiver is considered to remove the clock bias of each pseudolite. If the pseudolites are completely time-synchronized, the correction process from (10) to (12) is unnecessary. A correction term ξ from the reference receiver can be expressed in (10).

$$\xi^{12} \equiv \nabla_r^{12}\phi - \nabla_r^{12}d = \nabla_r^{12}N\lambda - \nabla^{12}b + \nabla_r^{12}\varepsilon', \tag{10}$$

where subscript r denotes the reference receiver and the distances from the reference receiver to each antenna are known parameters. Applying the correction term, (9) and (10) can be expressed as (11):

$$\begin{aligned}\nabla_u^{12}\phi' &\equiv \nabla_u^{12}\phi - \xi^{12} \\ &= \nabla_u^{12}d + \left(\nabla_r^{12}N\lambda - \nabla_u^{12}N\lambda\right) + \left(\nabla_r^{12}\varepsilon' - \nabla_u^{12}\varepsilon'\right) \\ &= \nabla_u^{12}d + \Delta\nabla_{ru}^{12}N\lambda + \Delta\nabla_{ru}^{12}\varepsilon',\end{aligned} \tag{11}$$

where

$$\Delta\nabla_{ru}^{jk}X \equiv \nabla_r^{jk}X - \nabla_u^{jk}X. \tag{12}$$

Equation (11) can be expressed in another form, as in (13).

$$\begin{aligned}\nabla_u^{12}\phi' + \mathbf{R}^1\cdot\mathbf{e_u^1} - \mathbf{R}^2\cdot\mathbf{e_u^2} - \Delta\nabla_{ru}^{12}N\lambda \\ = (\mathbf{e_u^1} - \mathbf{e_u^2})\cdot\mathbf{R_u} + \Delta\nabla_{ru}^{12}\varepsilon'.\end{aligned} \tag{13}$$

where $\mathbf{R^j}$ is the position of the j-th pseudolite antenna, $\mathbf{R_u}$ is the user position, and $\mathbf{e^j}$ denotes the line-of-sight unit vector from the receiver to the j-th pseudolite antenna.

Measurement equations for five pseudolite antennas are shown from (14) to (17).

$$\mathbf{z} \equiv \begin{bmatrix} \nabla_u^{12}\phi' + \mathbf{R^1}\cdot\mathbf{e_u^1} - \mathbf{R^2}\cdot\mathbf{e_u^2} - \Delta\nabla_{ru}^{12}N\lambda \\ \nabla_u^{23}\phi' + \mathbf{R^2}\cdot\mathbf{e_u^2} - \mathbf{R^3}\cdot\mathbf{e_u^3} - \Delta\nabla_{ru}^{23}N\lambda \\ \nabla_u^{34}\phi' + \mathbf{R^3}\cdot\mathbf{e_u^3} - \mathbf{R^4}\cdot\mathbf{e_u^4} - \Delta\nabla_{ru}^{34}N\lambda \\ \nabla_u^{45}\phi' + \mathbf{R^4}\cdot\mathbf{e_u^4} - \mathbf{R^5}\cdot\mathbf{e_u^5} - \Delta\nabla_{ru}^{45}N\lambda \\ h \end{bmatrix}, \tag{14}$$

$$\mathbf{H} \equiv \begin{bmatrix} \mathbf{e_u^1} - \mathbf{e_u^2} \\ \mathbf{e_u^2} - \mathbf{e_u^3} \\ \mathbf{e_u^3} - \mathbf{e_u^4} \\ \mathbf{e_u^4} - \mathbf{e_u^5} \\ 0\ 0\ 1 \end{bmatrix}, \tag{15}$$

$$\mathbf{v} \equiv \begin{bmatrix} \Delta\nabla_{ru}^{12}\varepsilon' & \Delta\nabla_{ru}^{23}\varepsilon' & \Delta\nabla_{ru}^{34}\varepsilon' & \Delta\nabla_{ru}^{45}\varepsilon' & \varepsilon_h \end{bmatrix}^T, \tag{16}$$

$$\mathbf{z} = \mathbf{H}\cdot\mathbf{R_u} + \mathbf{v}, \tag{17}$$

where h is a known parameter of height. If cycle ambiguity integers in (14) are solved correctly, the estimated user position ($\hat{\mathbf{R}}_\mathbf{u}$) can be calculated based on the least-squares solution of (18) with an iterative process updating the

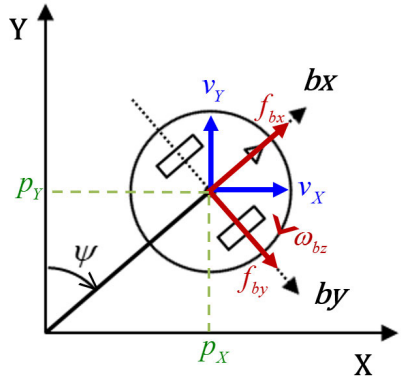

FIGURE 3. Local frame (X,Y) and body frame (bx,by) coordinates.

line-of-sight vectors. The initial user position for the iteration is set randomly near the origin, whose standard deviations are one centimeter for each axis. All iteration processes have been converged if cycle ambiguities are correct.

$$\hat{\mathbf{R}}_\mathbf{u} = (\mathbf{H}^\mathbf{T}\mathbf{H})^{-1}\mathbf{H}^\mathbf{T}\mathbf{z}. \tag{18}$$

The process for cycle ambiguity resolution will be presented in section II.D.

Doppler measurements are used to calculate the user velocity. Because the multiple pseudolites are not synchronized, the measurements from a reference receiver whose velocity is zero are considered as (19).

$$\nabla_u^{12}\dot{\phi}' \equiv \nabla_u^{12}\dot{\phi} - \dot{\xi}^{12} = \nabla_u^{12}\dot{\phi} - \nabla_r^{12}\dot{\phi}, \tag{19}$$

where $\dot{\phi}$ is a Doppler measurement. The measurement matrix for the five-antenna case is derived as (20):

$$\dot{\mathbf{z}} \equiv \left[\, \nabla_u^{12}\dot{\phi}' \;\; \nabla_u^{23}\dot{\phi}' \;\; \nabla_u^{34}\dot{\phi}' \;\; \nabla_u^{45}\dot{\phi}' \;\; 0 \,\right]^T, \tag{20}$$

because the antenna has a fixed position, and the height difference between the antenna and the user is fixed for 2D positioning. Then, the calculated user velocity is given as (21).

$$\hat{\dot{\mathbf{R}}}_\mathbf{u} = (\mathbf{H}^\mathbf{T}\mathbf{H})^{-1}\mathbf{H}^\mathbf{T}\dot{\mathbf{z}} \tag{21}$$

C. IMU-AIDED POSITIONING

In this study, the low-cost IMUs loaded in smartphones are utilized to show the potential of improved positioning accuracy. A simplified 2D navigation equation is considered throughout this study to show its feasibility.

Two coordinate frames are considered for positioning as shown in Fig. 3. Capital letters **X** and **Y** denote the local frame, and they are positioned at subscript for the position (p_X, p_Y) and velocity (v_X, v_Y). *bx*, *by,* and *bz* are the X, Y, and Z axes of the body frame, respectively, and they are positioned at subscript for the accelerometer (f_{bx}, f_{by}) and gyroscope (w_{bz}). *bx* is along the forward direction of the rover, and ψ is a heading clockwise from the **Y** axis.

A loosely coupled Kalman filter is incorporated, as in the block diagram of Fig. 4. In Fig. 4, superscripts of – and + mean *a priori* and *a posteriori* estimates, respectively. Subscript m represents measurement, and $\mathbf{z_m}$ is a measurement vector of default form from the Mosaic system as defined below:

$$\mathbf{z_m} = \left[\, \bar{p}_Y \;\; \bar{p}_X \;\; \bar{v}_Y \;\; \bar{v}_X \;\; \bar{\psi} \,\right]^T, \tag{22}$$

where bar or hat over the state means the measured state from sensors or the estimated state after filtering, respectively. Positions and velocities in (22) are from (18) and (21), respectively.

Since only simplified 2D positioning is considered in this study, accelerometers for the x and y axes and a gyroscope for the z axis in the body frame are considered for IMU measurements. Modeling of the IMU measurements is shown in (23) and (24):

$$\bar{f} = f + b_f + w_f, \quad \text{and} \tag{23}$$

$$\bar{\omega} = \omega + b_\omega + w_\omega, \tag{24}$$

where f and ω denote the acceleration and angular rate, respectively; b_f and b_ω are accelerometer and gyroscope biases, respectively; and w_f and w_ω are sensor noises for accelerometer and gyroscope, respectively. In this study, a state vector is defined as in (25).

$$\mathbf{x} = \left[\, p_Y \quad p_X \quad v_Y \quad v_X \quad \psi \quad b_{f_{bx}} \quad b_{f_{by}} \quad b_{\omega_{bz}} \,\right]^T \tag{25}$$

The nonlinear state equation for simplified 2D navigation is derived as follows:

$$\dot{\mathbf{x}} = f(\mathbf{x}, \mathbf{w}), \quad \text{and} \tag{26}$$

$$f(\mathbf{x}, \mathbf{w}) = \begin{bmatrix} v_Y \\ v_X \\ (\bar{f}_{bx} - b_{f_{bx}} - w_{f_{bx}})\cos\psi - (\bar{f}_{by} - b_{f_{by}} - w_{f_{by}})\sin\psi \\ (\bar{f}_{bx} - b_{f_{bx}} - w_{f_{bx}})\sin\psi + (\bar{f}_{by} - b_{f_{by}} - w_{f_{by}})\cos\psi \\ \bar{\omega}_{bz} - w_{\omega_{bz}} \\ w_{b_{f_{bx}}} \\ w_{b_{f_{by}}} \\ 0 \end{bmatrix}, \tag{27}$$

where

$$\mathbf{w} = \left[\, w_{f_{bx}} \quad w_{f_{by}} \quad w_{\omega_{bz}} \quad w_{b_{f_{bx}}} \quad w_{b_{f_{by}}} \,\right]^T. \tag{28}$$

According to (27), the bias drift of the gyroscope is assumed to be 0, because it can be considered stable during the experiments. To improve the positioning performance, parameters for the filter are tuned by considering the motion characteristics of the two-wheeled mobile robot. The movement of the two-wheeled rover is a combination of moving forward and rotating in place. Since these two movements have different features, two sets of process noises in (28) are applied to each movement for filtering. Movements can be classified using command history. In addition, it was discovered that the noise levels of the sensors are dependent

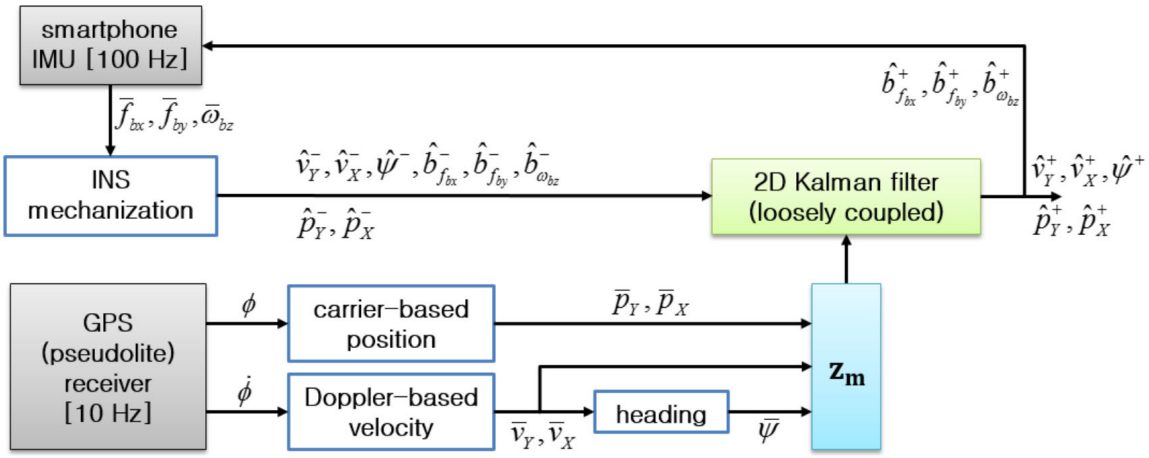

FIGURE 4. Block diagram of the Kalman filter for IMU-combined positioning.

on the speed of the rover because higher speeds increased the vibration of the rover. Therefore, the speed of the rover is also considered for processing the noises. The detailed methodology and tuning processes are found in [21].

The linearized state equation is expressed as follows:

$$\delta\dot{\mathbf{x}} = \mathbf{F}\delta\mathbf{x} + \mathbf{G}\mathbf{w}, \quad \text{where} \tag{29}$$

$$\mathbf{F} \equiv \frac{\partial \mathbf{f}(\mathbf{x}, \mathbf{w})}{\partial \mathbf{x}}, \quad \text{and} \tag{30}$$

$$\mathbf{G} \equiv \frac{\partial \mathbf{f}(\mathbf{x}, \mathbf{w})}{\partial \mathbf{w}}. \tag{31}$$

The extended Kalman filter is composed using the linearized system equation of (29) and the measurement equation of (32). Time updates are performed using IMU measurements at 100 Hz for propagation, and the measurement update is conducted using the Mosaic position and velocity information rates of 10 Hz.

$$\mathbf{z_m} = \begin{bmatrix} 1 & 0 & 0 & 0 & 0 & 0 & 0 & 0 \\ 0 & 1 & 0 & 0 & 0 & 0 & 0 & 0 \\ 0 & 0 & 1 & 0 & 0 & 0 & 0 & 0 \\ 0 & 0 & 0 & 1 & 0 & 0 & 0 & 0 \\ 0 & 0 & 0 & 0 & 1 & 0 & 0 & 0 \end{bmatrix} \mathbf{x} + \mathbf{v_m} \tag{32}$$

Characteristics of the two-wheeled rover are also applied for measurement updates based on [21]. Because the movement of the rover is a combination of moving forward and rotating in place, additional constraints for the measurement update process are considered. During forward movement, zero side velocity is considered, as in (33) using subscript sv, and the constraint of (34) is applied during rotation in place with zero velocity using subscript zv.

$$\begin{aligned} \mathbf{z_{m,sv}} &\equiv \begin{bmatrix} 0 & 0 & -\sin\psi & \cos\psi & 0 & 0 & 0 & 0 \end{bmatrix} \mathbf{x} + \mathbf{v_{m,sv}} \\ &= 0 \end{aligned} \tag{33}$$

$$\mathbf{z_{m,zv}} \equiv \begin{bmatrix} 0 & 0 & 1 & 0 & 0 & 0 & 0 & 0 \\ 0 & 0 & 0 & 1 & 0 & 0 & 0 & 0 \end{bmatrix} \mathbf{x} + \mathbf{v_{m,zv}} = \begin{bmatrix} 0 \\ 0 \end{bmatrix} \tag{34}$$

When a Mosaic measurement update is available, it is applied together with a zero velocity update or a zero side velocity update for filtering. If there is no Mosaic measurement update, only a zero velocity update or a zero side velocity update is applied.

Measurement noises $\mathbf{v_m}$ in (32) are generated using the error levels of the measurements and the DOP value of the Mosaic system, and $\mathbf{v_{m,sv}}$ and $\mathbf{v_{m,zv}}$ are tuned empirically. Detailed processes and methodology are found in [21].

D. CYCLE AMBIGUITY RESOLUTION

Ambiguity resolution can be defined as a process of selecting the true solution from the potential candidates that are generated due to the integer-cycle ambiguity. The number of cycle ambiguities of the Mosaic system is geometrically bounded as in (8). In addition, the total number of cycles of ambiguity can be reduced using the least-squares ambiguity search technique (LSAST), partitioning the measurements into a primary group and another secondary group [22]. The measurement equations for the primary group can be defined as (35) and (36) because 2D positioning is only available using three pseudolite antennas:

$$\mathbf{z_p} \equiv \begin{bmatrix} \nabla_u^{12}\phi' + \mathbf{R^1} \cdot \mathbf{e_u^1} - \mathbf{R^2} \cdot \mathbf{e_u^2} - \Delta\nabla_{ru}^{12} N\lambda \\ \nabla_u^{23}\phi' + \mathbf{R^2} \cdot \mathbf{e_u^2} - \mathbf{R^3} \cdot \mathbf{e_u^3} - \Delta\nabla_{ru}^{23} N\lambda \\ h \end{bmatrix}, \quad \text{and} \tag{35}$$

$$\mathbf{H_p} \equiv \begin{bmatrix} \mathbf{e_u^1} - \mathbf{e_u^2} \\ \mathbf{e_u^2} - \mathbf{e_u^3} \\ 0\ 0\ 1 \end{bmatrix}, \tag{36}$$

where the subscript p means the primary group. Positioning by the primary group is presented as (37).

$$\hat{\mathbf{R}}_{\mathbf{u,p}} = (\mathbf{H_p^T H_p})^{-1} \mathbf{H_p^T z_p}. \tag{37}$$

The integer ambiguities of the secondary group can be fixed depending on the calculated position of the primary measurement group as (38) for the five-antenna case:

$$\begin{bmatrix} \Delta\nabla_{ru}^{34} N \\ \Delta\nabla_{ru}^{45} N \end{bmatrix} = \text{round}$$

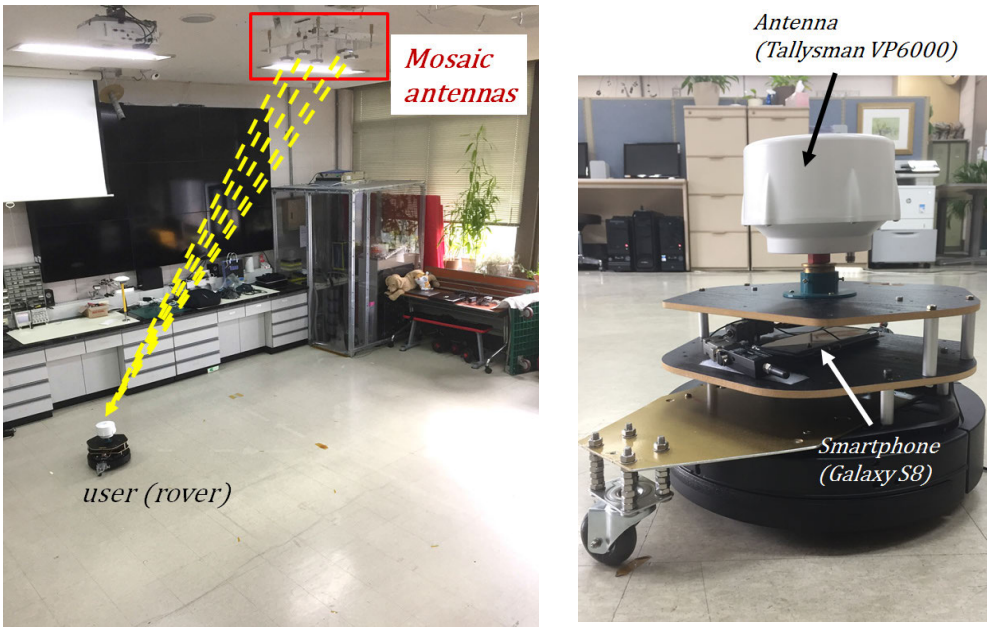

FIGURE 5. (a) Indoor test environment and (b) user (rover) configuration.

TABLE 1. Positions of Pseudolite antennas.

Pseudolite	X-position (m)	Y-position (m)	Z-position (m)
PRN 1	0	0.243	3.047
PRN 2	0.231	0.075	3.047
PRN 3	0.143	-0.196	3.047
PRN 4	-0.143	-0.196	3.047
PRN 5	-0.231	0.075	3.047

$$\left(\frac{1}{\lambda}\left(\begin{bmatrix}\nabla_u^{34}\phi' + \mathbf{R^3}\cdot\mathbf{e_u^3} - \mathbf{R^4}\cdot\mathbf{e_u^4}\\ \nabla_u^{45}\phi' + \mathbf{R^4}\cdot\mathbf{e_u^4} - \mathbf{R^5}\cdot\mathbf{e_u^5}\end{bmatrix} - \begin{bmatrix}\mathbf{e^3}-\mathbf{e^4}\\ \mathbf{e^4}-\mathbf{e^5}\end{bmatrix}\hat{\mathbf{R}}_{\mathbf{u,p}}\right)\right). \tag{38}$$

Therefore, only the cycle ambiguities in the primary group need to be fixed for positioning. If the antenna baseline length is about 1.5 λ, the total number of candidates for the system is only nine ($3^2 = 9$), because the number of candidates for each SDCP is three according to (8), and there are two integer ambiguities in the primary group. In this case, the nine candidates can be expressed as (39) and (40):

$$\begin{aligned}&\left\langle\left(\Delta\nabla_{ru}^{12}N,\ \Delta\nabla_{ru}^{23}N\right)\right\rangle\\ &= \left\{\left(\Delta\nabla_{ru}^{12}\tilde{N}-1, \Delta\nabla_{ru}^{23}\tilde{N}-1\right),\right.\\ &\quad\left(\Delta\nabla_{ru}^{12}\tilde{N}, \Delta\nabla_{ru}^{23}\tilde{N}-1\right), \left(\Delta\nabla_{ru}^{12}\tilde{N}+1, \Delta\nabla_{ru}^{23}\tilde{N}-1\right),\\ &\quad\left(\Delta\nabla_{ru}^{12}\tilde{N}-1, \Delta\nabla_{ru}^{23}\tilde{N}\right), \left(\Delta\nabla_{ru}^{12}\tilde{N}, \Delta\nabla_{ru}^{23}\tilde{N}\right),\\ &\quad\left(\Delta\nabla_{ru}^{12}\tilde{N}+1, \Delta\nabla_{ru}^{23}\tilde{N}\right), \left(\Delta\nabla_{ru}^{12}\tilde{N}-1, \Delta\nabla_{ru}^{23}\tilde{N}+1\right),\\ &\quad\left(\Delta\nabla_{ru}^{12}\tilde{N}, \Delta\nabla_{ru}^{23}\tilde{N}+1\right), \left.\left(\Delta\nabla_{ru}^{12}\tilde{N}+1, \Delta\nabla_{ru}^{23}\tilde{N}+1\right)\right\},\end{aligned} \tag{39}$$

where

$$\Delta\nabla_{ru}^{jk}\tilde{N} \equiv \text{round}\left(\nabla_u^{jk}\phi'/\lambda\right). \tag{40}$$

It is geometrically guaranteed that the true integer set is within (39); therefore a residual-based ratio test, which is widely utilized to fix the cycle ambiguity [23]–[26], is applied in this study. According to each candidate in (39), each

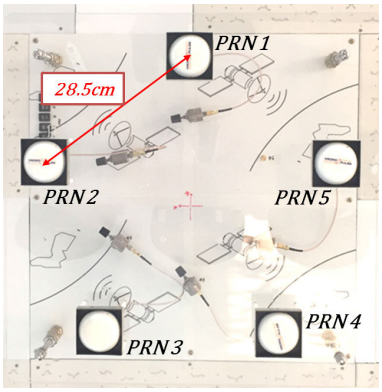

FIGURE 6. Pseudolite antenna array.

TABLE 2. Reference antenna position.

X-position (m)	Y-position (m)	Z-position (m)
-0.155	-1.498	0.469

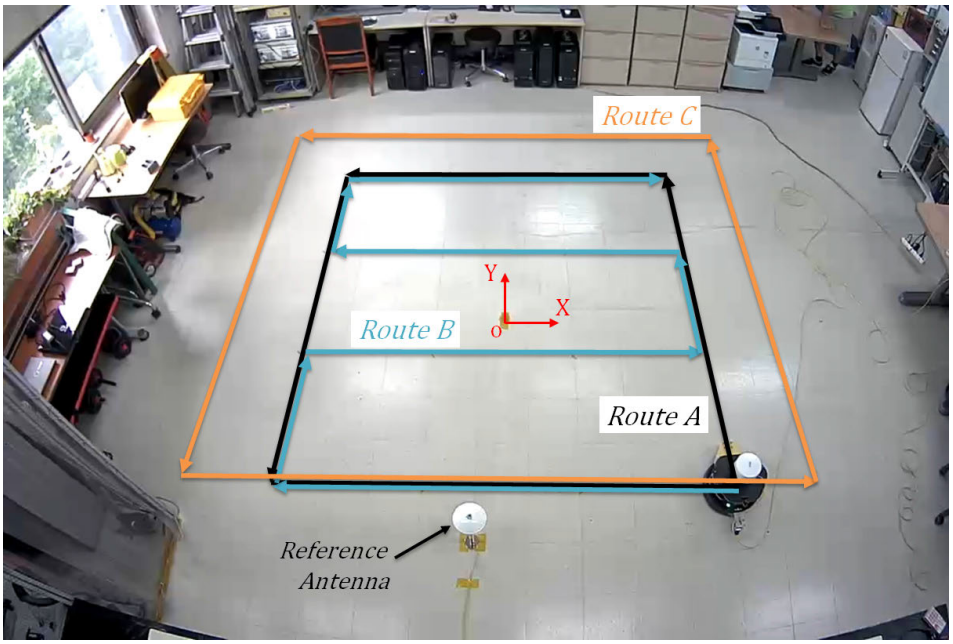

FIGURE 7. Three experimental routes.

measurement residual can be calculated as in (41) using the integer ambiguities of the secondary group calculated using (40).

$$\delta \mathbf{z} \equiv \mathbf{H} \cdot \hat{\mathbf{R}}_{\mathbf{u}} - \mathbf{z} \tag{41}$$

The squared sum of errors (SSE) is calculated using the residuals, as in (42).

$$\Omega \equiv \delta \mathbf{z}^{\mathbf{T}} \cdot \delta \mathbf{z}. \tag{42}$$

It is known that the SSE has a chi-square statistical distribution if the measurement residual has a Gaussian distribution [25]. The basic concept of the ratio f-test is that the ratio of two chi-square distributions has a f-distribution [23]. The ratio of the two SSEs, whose denominator is the minimum SSE among the candidates, is compared with a certain threshold, which is generated using the f-distribution in general. Practically, the accumulated SSEs through epochs as in (43) also can be applied for the ratio test [24].

$$\Phi_k(t) \equiv \sum_{i=1}^{t} \Omega_k(i), \tag{43}$$

where i is an epoch from 1 to the current t and subscript k is an index of candidates from 1 to 9 as described in (39). This study also utilizes the accumulated SSEs of each candidate for the ratio test:

$$\frac{\Phi_l(t)}{\Phi_m(t)} > \Lambda, \tag{44}$$

where subscript l is an index of accumulated SSEs from 1 to 9, except for m, which is an index of the minimum accumulated SSE. If the ratio is bigger than the threshold value of Λ, the candidate of index l is considered to be a false solution. The threshold value for the ratio test is set empirically through experiments.

During the cycle ambiguity resolution process, two additional criteria are considered. The first one is the convergence of the calculations of the positions in (21) and (37). An iterative process is required for the positioning estimation until the calculated positions converge. However, a calculated position can diverge or oscillate for some false integer-ambiguity cases. Therefore, non-converged candidates are considered as false candidates. The second criterion considers the expected positioning area where the user can possibly be located. One of the characteristics of the Mosaic system, which is different when compared to the conventional carrier-phase-based GNSS, is that potential solutions from false candidates are distinct from each other [6]. Therefore, positioning results by some false candidates can be located outside of the expected indoor area. They can be excluded from the candidates.

III. EXPERIMENTAL RESULTS

A. EXPERIMENTAL CONFIGURATION

Experiments for performance analyses of positioning accuracy and cycle ambiguity resolution were conducted in office and lab environments. The test environment was not cleaned for facilitating a pure analysis of positioning accuracy. Instead, it represented what was expected in an actual office environment. Because the structure of the building was steel frame and the main material of the walls was concrete block, it was not favorable for correcting multipath errors. In addition, there were various objects in the room, such as bookshelves, tables, drawers, metal window blinds, and other metal structures, as depicted in Fig. 5.

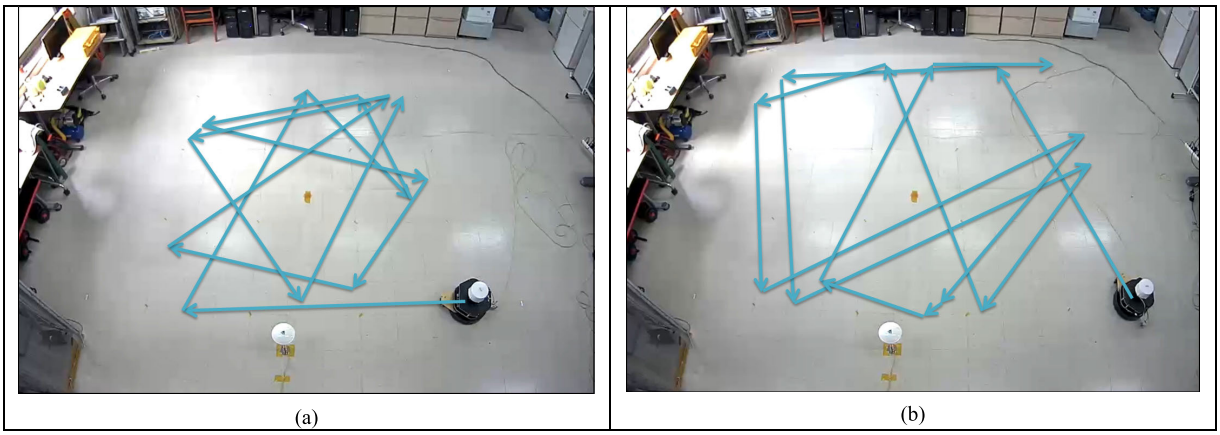

FIGURE 8. Movements in scenarios 4 and 5: (a) scenario 4 and (b) scenario 5.

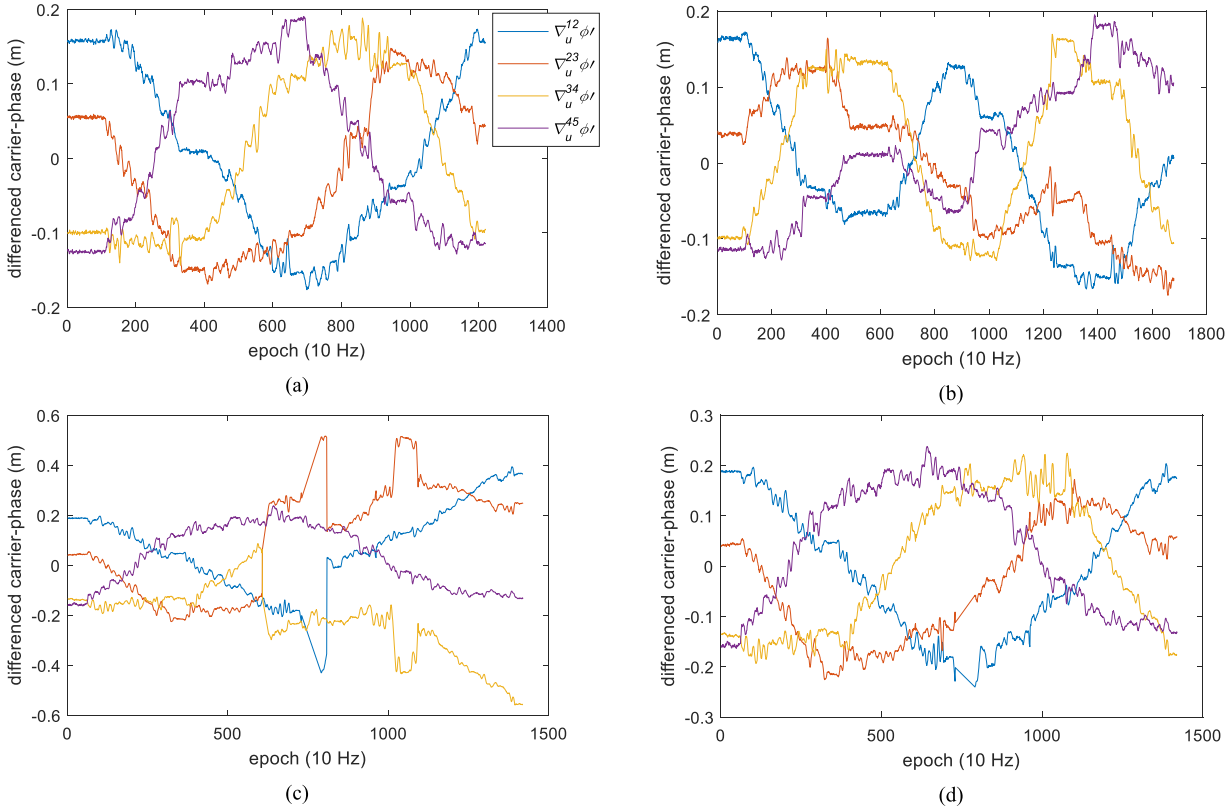

FIGURE 9. Differenced carrier-phase measurements for scenarios: (a) scenario 1, (b) scenario 2, (c) scenario 3 before cycle slip compensation, and (d) scenario 3 after cycle slip compensation.

As depicted in Fig. 5 (a), the pseudolite antenna array was installed on the ceiling of the room. An IN-200 series pseudolite antenna array broadcasted GPS signals using 1023 Gold code on an L1 carrier (1575.42 MHz). A PRN of one to five GPS signals was set to each pseudolite with radio technical communication for maritime service pulsing. The user was a two-wheeled mobile rover on the floor. Its speed was about 15 cm/s. A Tallysman VP6000 antenna and a GPS receiver developed by Telace Inc. were used for the rover. The same receiver was also utilized for reference. The GPS receiver generated 10 Hz measurement signals. In addition, a Galaxy S8 smartphone by Samsung Electronics was installed on the rover to acquire the IMU sensor data: x- and y-axis accelerometers and a z-axis gyroscope for 2D positioning.

The pseudolite antenna array has a pentagon shape, as shown in Fig. 6. The pentagon shape provided almost uniform positioning performance around the antenna and good performance of cycle ambiguity resolution according to previous research [8]. The positions of the antennas are described in Table 1. The geometrical phase center is considered as the position of the antennas. The distance between antennas is 28.5 cm $=$ 1.5 λ of the L1 carrier signal.

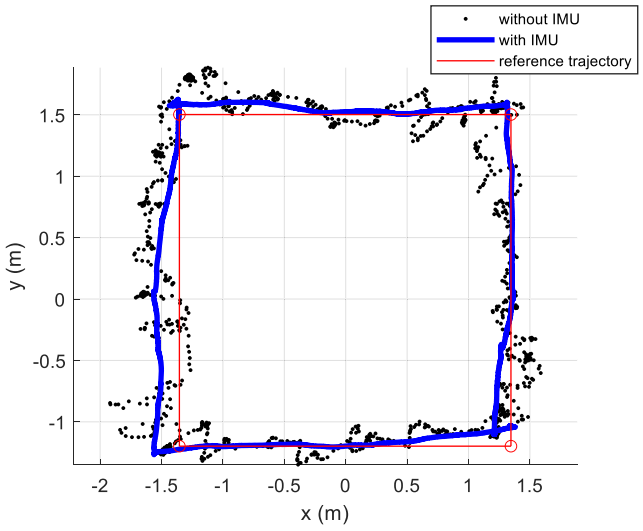

FIGURE 10. Positioning results of scenario 1.

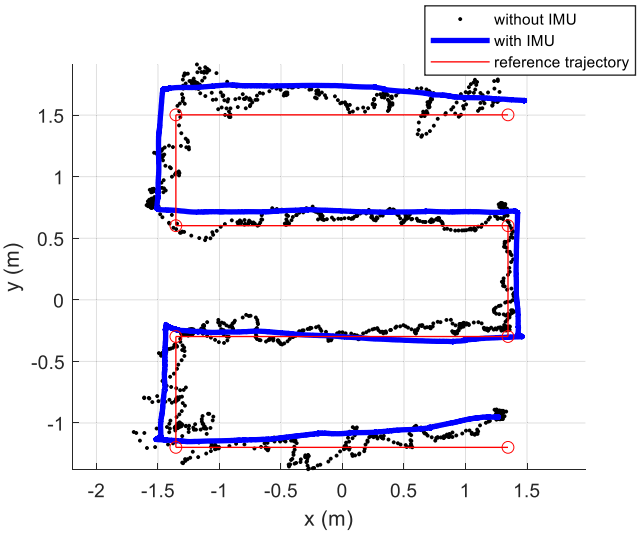

FIGURE 11. Positioning results of scenario 2.

In Fig. 7, the origin of the local coordinates and the position of the reference receiver are displayed. The reference position is expressed in Table 2. A total of five experiment scenarios are described in this study. In these scenarios, three routes were considered, as depicted in Fig. 7. The five experiment scenarios are as follows:

- Scenario 1: The rover goes around following route A.
- Scenario 2: The rover follows route B.
- Scenario 3: The rover goes around following route C.
- Scenario 4: The rover randomly moves inside of the route A boundary.
- Scenario 5: The rover randomly moves inside of the route C boundary.

Route A is set as an ordinary square trajectory. Route B is considered to display the positioning results inside of route A. Route B also can depict the results below the transmitter. Route C is additionally considered for the investigation of positioning performance near surrounding objects. It is expected that route C has bad DOP and large multipath errors compared to route A or B. For the performance analysis of cycle ambiguity resolution, scenario 4 and 5 which have random movements are additionally considered to present generalized performance. The random movements of scenarios 4 and 5 are roughly shown in Fig. 8.

Scenarios from 1 to 3 are used for the analysis of positioning performance. The initial headings of these scenarios are assumed to be roughly known. All scenarios from 1 to 5 are utilized for the analysis of the cycle ambiguity resolution.

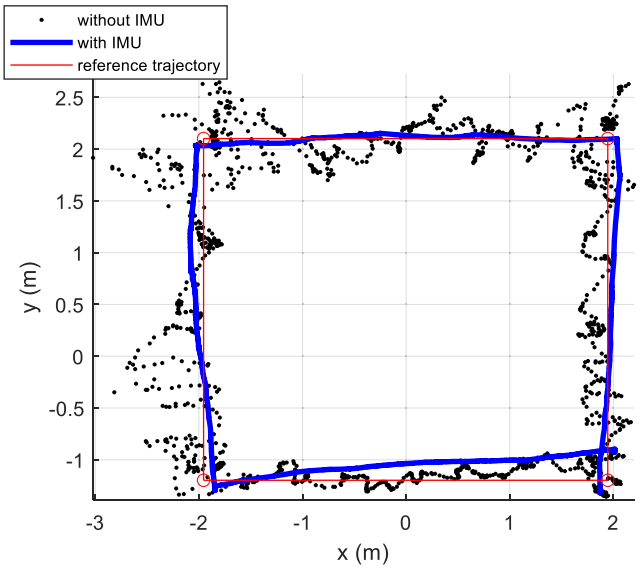

FIGURE 12. Positioning results of scenario 3.

TABLE 3. Positioning accuracy in three scenarios.

	Positioning accuracy (meter, RMS[a])		
	Scenario 1	Scenario 2	Scenario 3
Mosaic without IMU	0.196	0.181	0.242
Mosaic with IMU	0.136	0.163	0.157

[a]Root mean square

B. POSITIONING PERFORMANCE

For the performance analysis of the positioning accuracy, two solutions were calculated and compared. The first one was the results obtained by using only the Mosaic system (18) with carrier-phase measurements. The second one was the positioning results obtained by combining the Mosaic system and analysis of the IMU sensor data from the smartphone.

Differenced carrier-phase measurements as per (11) for each scenario are depicted in Fig. 9. In this section, it is assumed that cycle ambiguity problems are solved using the measurements of the first epoch and the known initial position. Analyses of the general cycle ambiguity problem without knowing the initial position are described in the next section.

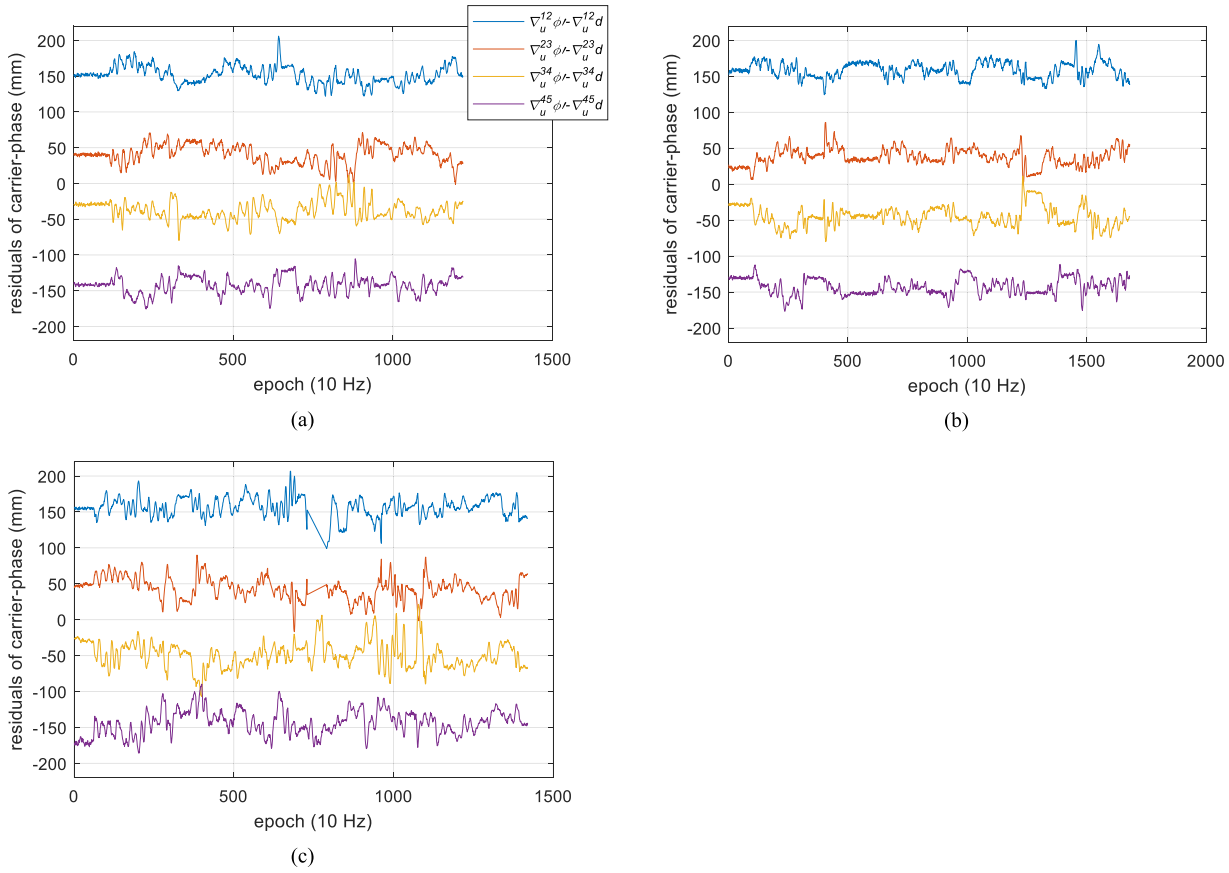

FIGURE 13. Residuals of differenced carrier-phase measurements for scenarios: (a) scenario 1, (b) scenario 2, and (c) scenario 3. Note that differenced residuals between one and two (blue line), two and three (red line), three and four (yellow line), and four and five (purple line) have been offset by +150 mm, +50 mm, -50 mm, and -150 mm respectively for better readability.

TABLE 4. Residual errors of differenced carrier-phase measurements.

Differenced measurements	Residual errors (mm, RMS)		
	Scenario 1	Scenario 2	Scenario 3
$\nabla_u^{12}\phi' - \nabla_u^{12}d$	12.5	14.2	15.3
$\nabla_u^{23}\phi' - \nabla_u^{23}d$	16.4	17.0	17.2
$\nabla_u^{34}\phi' - \nabla_u^{34}d$	18.0	14.8	18.4
$\nabla_u^{45}\phi' - \nabla_u^{45}d$	14.2	13.8	18.3
All Measurements	15.3	14.9	17.3

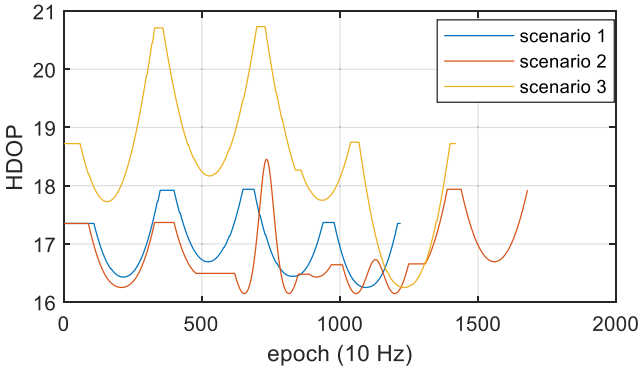

FIGURE 14. HDOP variations according to scenarios one, two, and three.

During these experiments, only scenario 3 had an issue with cycle slip, as shown in Fig. 9 (c), because the scenario had a poor route for multipath error: near the wall or other furniture and far from the transmitter. A total of five cycle slips occurred at five measurements in one round. In this study, cycle slip detection and compensations were conducted manually during post-processing. The differenced measurement after compensation is depicted in Fig. 9 (d). In-depth research about cycle slips remains to be conducted in the future, along with considerations of the detection threshold and real-time compensation.

The positioning results of scenarios 1, 2, and 3 are displayed in Fig. 10, Fig. 11, and Fig. 12, respectively.

The positioning results using only the Mosaic system without IMU, that is, the black dots in Fig. 10, Fig. 11, and Fig. 12, are displayed and show that they generally follow the reference trajectories. However, they are highly cursive. In previous research [14], cursive noises of the Mosaic system were geometrically dependent or were position-dependent mainly due to multipath errors. When the user rounded the

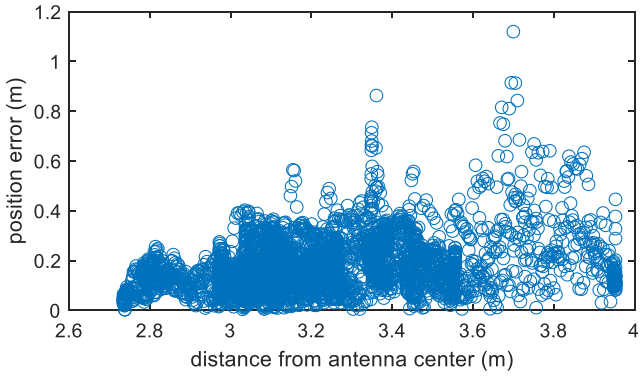

FIGURE 15. Relationship between the distance from antenna center and the positioning error.

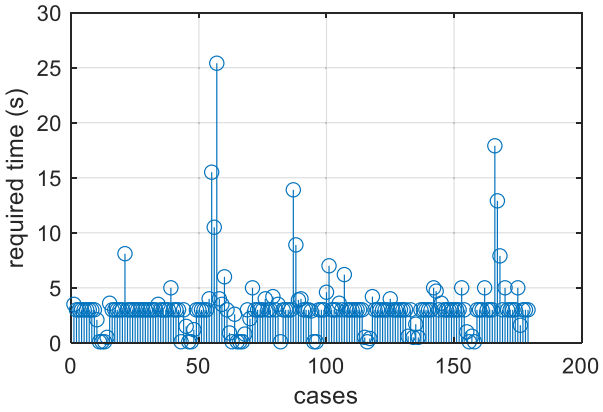

FIGURE 16. Required time for cycle ambiguity resolution.

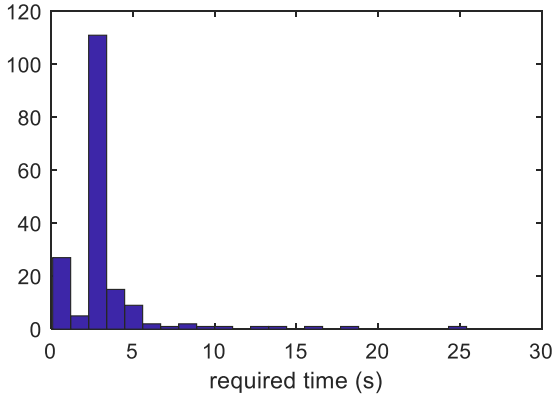

FIGURE 17. Histogram of required time for cycle ambiguity resolution.

route multiple times, the trajectories overlapped with the same curvature. Because the multipath error of carrier-phase measurement has a bounded size and varies along with the path position [27], [28], it was expected that an IMU-based filter could improve the positioning accuracy.

To show the feasibility of improved accuracy using a smartphone-based IMU, a simplified 2D Kalman filter was applied, as in section II.C; the results are displayed using blue lines in the figures. The results obtained by combining Mosaic with the IMU demonstrate that the noise of the trajectories is greatly decreased. The overall positioning inaccuracies for each scenario are described in Table 3: around 30.5% of the positioning error was decreased. The reference positions of the user were derived based on recorded videos and images.

Fig. 13 displays the residual errors of each differenced carrier-phase measurement for the first three scenarios, and the statistical residual errors in the root-mean-square are summarized in Table 4. Residuals were calculated based on (11) after eliminating cycle ambiguity integers. Most residual errors are within ±50 mm. According to previous studies, most of the measurement error is caused by multipath and phase-center variation of the antenna [14], [15]. It is reasonable that scenario 3 has the largest residual errors, because its trajectory is close to the surrounding objects causing large multipath errors.

Positioning error is also affected by the distance from the transmitter to the user because it is a natural characteristic of a single-transmitter-based positioning system. Regarding DOP, horizontal DOP (HDOP) is increased almost proportionally along the distance from the transmitter, as described in previous references [6], [15]. HDOP variations according to scenarios from 1 to 3 are depicted in Fig. 14. HDOPs were calculated using the reference trajectories. Scenario 3 has large HDOP values because its trajectory is farther from the transmitter than in scenarios 1 and 2. Large HDOP values are another reason that scenario 3 has the largest positioning error when the Mosaic-only case (without IMU) is considered.

The relationship between distance from the transmitter to the user and the positioning error in scenarios from 1 to 3 is depicted in Fig. 15. The result is in line with previous research [6] concluding that the maximum positioning error is almost proportional to the distance from the center of the antenna array.

HDOP values, shown in Fig. 14, vary from approximately 16 to 21, which are large variations. If pseudo-range measurements, whose noise-level is around one meter, are utilized for positioning, positioning errors can be up to tens of meters. This performance is inappropriate for indoor positioning. Therefore, precise measurements, such as carrier-phase, are essential for precise positioning.

TABLE 5. Required times for cycle ambiguity resolution.

Scenario	No. of cases	Average of required time (s)	Standard deviation of required time (s)	Ambiguity resolution within 5 s (%)
Scenario 1	20	2.45	1.19	100.0
Scenario 2	31	2.86	1.42	96.8
Scenario 3	24	4.37	5.63	83.3
Scenario 4	48	3.32	2.21	91.7
Scenario 5	56	3.41	2.72	94.6
All scenarios	179	3.31	2.91	93.3

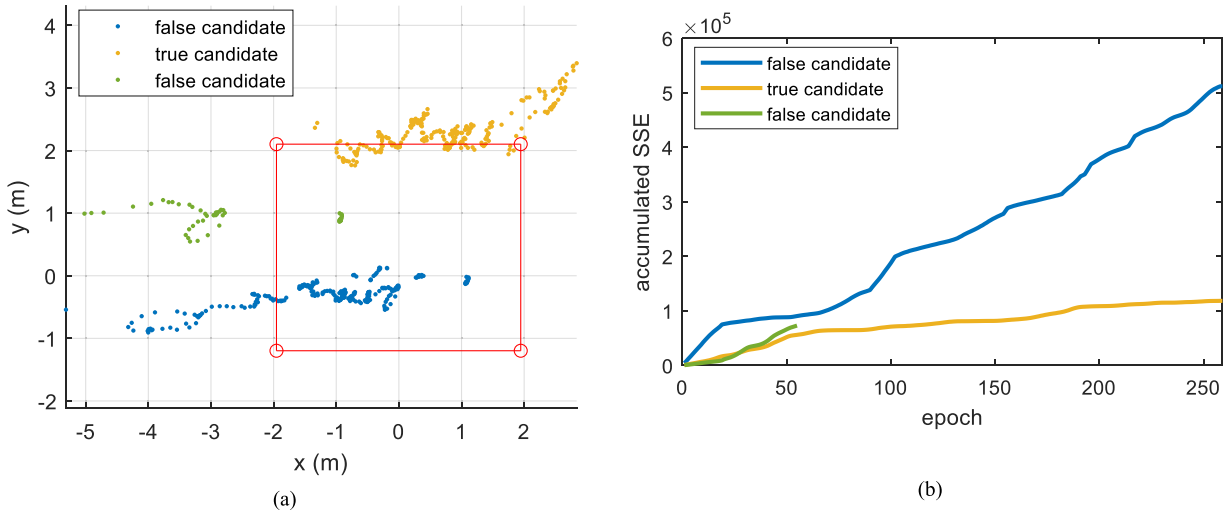

FIGURE 18. Positioning results and accumulated SSEs of candidates from the 351st epoch of scenario 3: (a) positioning results and (b) accumulated SSEs.

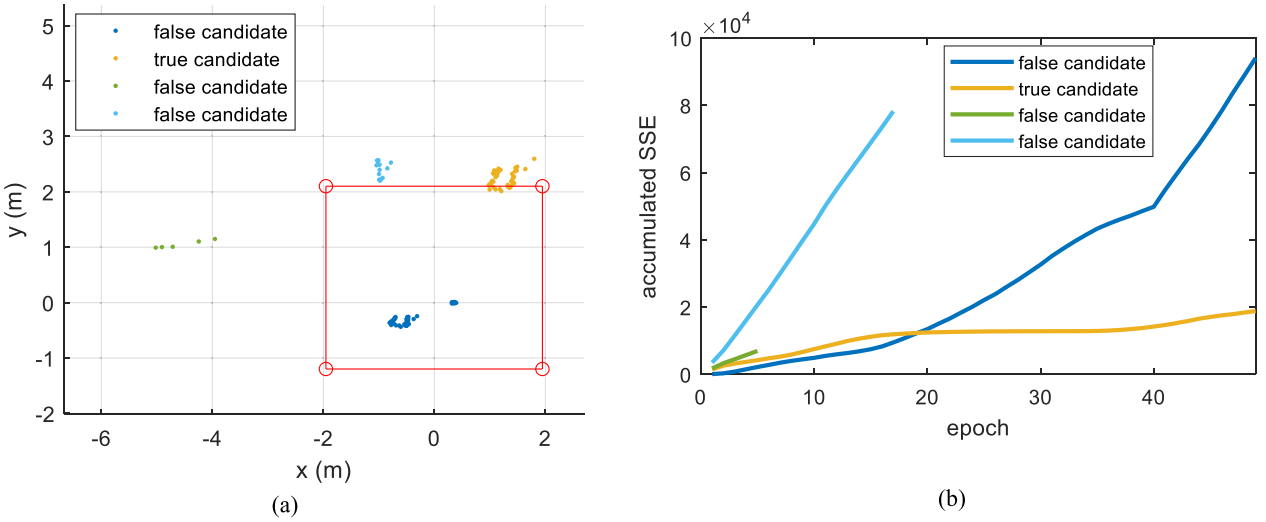

FIGURE 19. Positioning results and accumulated SSEs of candidates from 401st epoch of scenario 3: (a) positioning results and (b) accumulated SSEs.

According to DOP analysis in [15] and empirical experiences, the coverage of the Mosaic system is similar to the height of the antenna array. If the user moves over the boundary, the HDOP of the user increases considerably. One efficient way to improve the coverage is by combining it with round-trip signals, such as ultra-wideband (UWB) or round-trip time of Wi-Fi. There has been research showing that combining the Mosaic system with the measurement of round-trip time for aircraft application improved its coverage [6], [8].

C. PERFORMANCE OF CYCLE AMBIGUITY RESOLUTION

To investigate the performance of cycle ambiguity resolution, ambiguity resolution processes were started every 5 s for all scenarios; a total of 179 cases were considered. Because residual-based ambiguity resolution with LSAST was utilized, the number of candidates was nine, as described earlier. The accumulated ratio test, as in (44), convergence criteria, and expected positioning area were considered. During each process, the accumulated ratio test was begun after 3 s. The threshold value (Λ) of the test was set to five, empirically. The expected area was set from -5 to 5 meters on the X axis and -3 to 4 meters on the Y axis with a margin of a few meters to the experimental area.

The required times of ambiguity resolution for all cases are shown in Fig. 16. The histogram of the required time is described in Fig. 17.

Because the accumulated ratio test began after 3 s, the cycle ambiguity problems of most cases were resolved within 3 s. If the positioning results of candidates, except the true one, have not converged or been located out of the expected area, the cycle ambiguity can be solved in less than 3 s.

The performance of cycle ambiguity resolution for each scenario and the overall result are described in Table 5. Because there is no meaningful difference between scenarios, the overall result can represent the performance of cycle ambiguity resolution. The average required time for cycle

ambiguity resolution is 3.3 s. In addition, more than 93% of ambiguities are solved within 5 s.

According to Fig. 16, there was a case for which the required time was more than 20 s. It happened during scenario 3, starting at the 351st epoch. The positions of each candidate and the accumulated SSE from the 351st epoch are described in Fig. 18.

Only three candidates were judged to be valid from the beginning, because the other candidates were non-converged or out of the expected area. A false candidate, the green line in Fig. 18, was eliminated at the 55th epoch because its position was located out of the expected area. The other false candidate, the blue line, was also eliminated at the 259th epoch for the same reason. In this case, because the accumulated SSE of the false candidate increased very slowly, 259 epochs were required for ambiguity resolution.

Fig. 19 displays the positioning results and the accumulated SSEs by candidates from the 401st epoch of scenario 3. In this case, the green false candidate was eliminated considering the expected area, and the other two false candidates of blue and light blue were eliminated because their accumulated SSE ratios to the accumulated SSE of the minimum candidate were larger than the threshold value of five. Therefore, 49 epochs were required for ambiguity resolution when it began at the 401st epoch of scenario 3.

Comparing Fig. 18 and Fig. 19, considering the beginning epoch of scenario 3, the cycle ambiguities were resolved at the 610th and 450th epochs, respectively. The case starting at the 401st epoch was much faster than that starting at the 351st epoch. Therefore, it is recommended that users process the ambiguity resolution in parallel, beginning at different epochs, for fast and robust cycle ambiguity resolution.

IV. DISCUSSION AND CONCLUSION

In this study, the fundamental operability of the Mosaic system, a single-transmitter-based positioning system using an antenna array, for indoor environments, was investigated through experiments related to positioning accuracy and ambiguity resolution.

The configuration of the Indoor Mosaic system presented in this paper is similar to previous single-transmitter-based positioning systems [13], [15]; multi-channel pseudolite systems using an antenna array. References [13] and [15] considered an antenna baseline length smaller than a half of the wavelength. Therefore, solving the cycle ambiguity problem was unnecessary. However, the performance of positioning accuracy was not sufficient for precise indoor positioning with meter-level biases caused by high DOPs. To improve the geometric performance, the antenna baselines need to be enlarged. In preliminary experiments of this study, the performance change by increased antenna baseline length was investigated [14]. However, increasing the antenna baseline also results in the necessity of treating the cycle ambiguity problem, which had not been considered in previous studies.

There have been other studies using multi-channel pseudolite systems for precise indoor positioning [16], [17]. These studies installed pseudolite antennas far apart to achieve low DOP values. Because this system utilized Doppler measurements for positioning, there was no need for concern about the cycle ambiguity problem. Instead, the initial position of the user was required because the user position had been updated with the estimated velocity from the position of the previous epoch.

Unlike previous studies, the presented system in this paper fully considered the cycle ambiguity problem without the information about the user's initial position. It was verified by experiments considering various trajectories. The results demonstrated that most of the ambiguity problems can be solved very fast and accurately; more than 90% of the cycle ambiguities were solved accurately within 3.3 s. In addition, our results led us to recommend that users begin the ambiguity-clearing process in parallel at different epochs for fast ambiguity resolution.

For analysis of the positioning accuracy, the performance of a pure Mosaic system was evaluated with one in combination with IMUs. The positioning performance of the pure Mosaic system showed errors up to 25 cm in RMS, and its trajectories were very cursive. When the Mosaic system was combined with IMU sensors using a simplified 2D Kalman filter, the combined system's positioning had better accuracy with precise trajectories.

Further studies are considered for practical application of the system. Because the drawback of the Mosaic system is bad geometry resulting from close proximity between antennas, precise measurements such as carrier-phase are essential to achieve good accuracy performance. Therefore, effort to maintain the consistency of cycle ambiguity is required. Cycle slip problems, including detection and repair, need to be mitigated for practical real-time operation. Improving the process of cycle ambiguity validation also remains for future work. The coverage of this system is in relation to the height of the antenna array from the ground, unless an additional measurement such as the range measurement using round-trip signals is considered, in which case the coverage can be wider [6]. Further studies looking at combinations with other measurements also remain for future work. Presently, a smartphone can be utilized as a pseudolite receiver, using the GNSS chipset. It seems advantageous to study utilizing the smartphone as a receiver. In addition, there is no need to limit the application of single-transmitter-based positioning systems for the pseudolite. Different signal sources, such as UWB, Wi-Fi, and Bluetooth, have the potential to be used for the Mosaic concept.

ACKNOWLEDGMENT

The Institute of Engineering Research at Seoul National University provided research facilities for this work.

REFERENCES

[1] C. Kee and T. Lee, "Positioning system and method based on radio communication apparatus comprising multiple antenna," Republic of Korea Patent 10-0 979 623, Dec. 24, 2009.

[2] C. Kee and T. Lee, "Positioning system and method based on radio communication apparatus comprising multiple antenna," PCT Patent WO 137790 A1, Dec. 2, 2010.
[3] O.-J. Kim, C. Kim, J. Song, H. Yun, D. Kim, and C. Kee, "A new concept of APNT: MOSAIC/DME 3-D positioning with a single DME station," in *Proc. ITM ION*, Newport Beach, CA, USA, 2012, pp. 142–150.
[4] O.-J. Kim, C. Kim, J. Song, Y. Kim, and C. Kee, "Instantaneous ambiguity resolution of MOSAIC/DME: A single station based 3D positioning system for alternative PNT," in *Proc. ION GNSS*, Nashville, TN, USA, 2013, pp. 521–528.
[5] O.-J. Kim, C. Kim, J. Song, Y. Kim, and C. Kee, "The study of error sources for MOSAIC/DME system: A single station based positioning system for APNT," in *Proc. IEEE/ION Position, Location Navigat. Symp. (PLANS)*, Monterey, CA, USA, May 2014, pp. 855–863.
[6] O.-J. Kim, C. Kim, J. Song, T. Lee, B. Park, and C. Kee, "A single distance measuring equipment (DME) station-based positioning system for alternative position navigation and timing (APNT)," *Navigation*, vol. 62, no. 4, pp. 313–327, Dec. 2015, doi: 10.1002/navi.121.
[7] O.-J. Kim, "Single station-based precise positioning system using multi-antenna arrangement," Ph.D. dissertation, Dept. Mech. Aerosp. Eng., Seoul Natl Univ., Seoul, South Korea, 2018.
[8] O. Kim and C. Kee, "Single station-based precise positioning system: Multiple-antenna arrangement for instantaneous ambiguity resolution," *Navigation*, vol. 66, no. 4, pp. 747–768, Dec. 2019, doi: 10.1002/navi.329.
[9] H. Liu, H. Darabi, P. Banerjee, and J. Liu, "Survey of wireless indoor positioning techniques and systems," *IEEE Trans. Syst., Man, Cybern. C, Appl. Rev.*, vol. 37, no. 6, pp. 1067–1080, Nov. 2007, doi: 10.1109/TSMCC.2007.905750.
[10] L. Mainetti, L. Patrono, and I. Sergi, "A survey on indoor positioning systems," in *Proc. 22nd Int. Conf. Softw., Telecommun. Comput. Netw. (SoftCOM)*, Split, Croatia, Sep. 2014, pp. 111–120.
[11] R. F. Brena, J. P. García-Vázquez, C. E. Galván-Tejada, D. Muñoz-Rodriguez, C. Vargas-Rosales, and J. Fangmeyer, "Evolution of indoor positioning technologies: A survey," *J. Sensors*, vol. 2017, pp. 1–21, Mar. 2017, doi: 10.1155/2017/2630413.
[12] B. D. Elrod and A. J. Van Dierendonck, "Pseudolites," in *Global Positioning System: Theory and Applications*, vol. 2, B. W. Parkinson, J. J. Spilker, Jr., P. Axelrad, and P. Enge, Eds. Washington, DC, USA: American Institute of Aeronautics and Astronautics, Inc., 1996, ch. 2, pp. 51–78.
[13] C. Kim, O.-J. Kim, T. Lee, and C. Kee, "Indoor positioning system using single pseudolite with multiple antenna," in *Proc. ITM ION*, Newport Beach, CA, USA, 2012, pp. 1089–1097.
[14] O.-J. Kim, B. Shin, C. Kee, C. Kim, T. Lee, H. So, and G. Kim, "Single transmitter based precise positioning system using multiple antenna: Experimental tests," in *Proc. Int. Tech. Meeting Inst. Navigat.*, Reston, VN, USA, Feb. 2019, pp. 445–458.
[15] K. Fujii, Y. Sakamoto, W. Wang, H. Arie, A. Schmitz, and S. Sugano, "Hyperbolic positioning with antenna arrays and multi-channel pseudolite for indoor localization," *Sensors*, vol. 15, no. 10, pp. 25157–25175, Sep. 2015, doi: 10.3390/s151025157.
[16] X. Gan, B. Yu, L. Huang, R. Jia, H. Zhang, C. Sheng, G. Fan, and B. Wang, "Doppler differential positioning technology using the BDS/GPS indoor array pseudolite system," *Sensors*, vol. 19, no. 20, p. 4580, Oct. 2019, doi: 10.3390/s19204580.
[17] X. Gan, B. Yu, X. Wang, Y. Yang, R. Jia, H. Zhang, C. Sheng, L. Huang, and B. Wang, "A new array pseudolites technology for high precision indoor positioning," *IEEE Access*, vol. 7, pp. 153269–153277, Oct. 2019, doi: 10.1109/ACCESS.2019.2948034.
[18] X. Li, P. Zhang, J. Guo, J. Wang, and W. Qiu, "A new method for single-epoch ambiguity resolution with indoor pseudolite positioning," *Sensors*, vol. 17, no. 4, p. 921, Apr. 2017, doi: 10.3390/s17040921.
[19] Y. Zhao, P. Zhang, J. Guo, X. Li, J. Wang, F. Yang, and X. Wang, "A new method of high-precision positioning for an indoor pseudolite without using the known point initialization," *Sensors*, vol. 18, no. 6, p. 1977, Jun. 2018, doi: 10.3390/s18061977.
[20] P. Misra and P. Enge, *Global Positioning System: Signals, Measurements, and Performance*, 2nd ed. Lincoln, MA, USA: Ganga-Jamuna Press, 2010.
[21] D. Hong, "Smartphone based cycle slip detection for wheeled mobile robot navigation," M.S. thesis, Dept. Mech. and Aerosp. Eng., Seoul Natl Univ., Seoul, South Korea, 2020.
[22] R. Hatch, "Instantaneous ambiguity resolution," in *Proc. Kinematic Syst. Geodesy, Surveying, Remote Sens.*, Edmonton, AB, Canada, 1991, pp. 299–308.
[23] S. Han, "Quality-control issues relating to instantaneous ambiguity resolution for real-time GPS kinematic positioning," *J. Geodesy*, vol. 71, no. 6, pp. 351–361, May 1997, doi: 10.1007/s001900050103.
[24] C. Kee, D. Kim, and J. Jang, "Efficient ambiguity search technique using separated decision variables," *J. Navigat.*, vol. 60, no. 1, pp. 147–157, Jan. 2007, doi: 10.1017/S0373463307003992.
[25] P. J. G. Teunissen and S. Verhagen, "The GNSS ambiguity ratio-test revisited: A better way of using it," *Surv. Rev.*, vol. 41, no. 312, pp. 138–151, Apr. 2009, doi: 10.1179/003962609X390058.
[26] S. Verhagen and P. J. G. Teunissen, "The ratio test for future GNSS ambiguity resolution," *GPS Solutions*, vol. 17, no. 4, pp. 535–548, Oct. 2013, doi: 10.1007/s10291-012-0299-z.
[27] L. Lau and P. Cross, "Development and testing of a new ray-tracing approach to GNSS carrier-phase multipath modelling," *J. Geodesy*, vol. 81, no. 11, pp. 713–732, Oct. 2007, doi: 10.1007/s00190-007-0139-z.
[28] E. D. Kaplan and C. J. Hegarty, "Interference, multipath, and scintillation," in *Understanding GPS: Principles and Applications*, 2nd ed. Norwood, MA, USA: Artech House, 2006, ch. 6, pp. 243–299.

O-JONG KIM received the B.S., master's, and Ph.D. degrees from Seoul National University, South Korea, in 2011, 2013, and 2018, respectively. Since 2018, he has been a Ph.D. Researcher with the Institute of Advanced Aerospace Technology, Seoul National University. He is currently a Ph.D. Researcher with the School of Mechanical and Aerospace Engineering, Seoul National University. His research interests include alternative PNT, indoor navigation, cycle ambiguity resolution, and space technologies, such as space GNSS receiver and the nano-satellite platform.

DANIEL HONG received the B.S. degree in mechanical and control engineering from Handong Global University. He is currently pursuing the M.S. degree with the GNSS Laboratory, Department of Aerospace Engineering, Seoul National University. His research interests are navigation and control of autonomous ground vehicles.

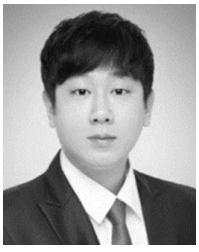

JUNGBEOM KIM received the B.S. and master's degrees from Seoul National University. He is currently pursuing the Ph.D. degree with the GNSS Laboratory, School of Mechanical and Aerospace Engineering, Seoul National University. His recent research interest is GPS/INS integrated navigation systems for autonomous vehicles.

TAIKJIN LEE received the B.S. and Ph.D. degrees from the School of Mechanical and Aerospace Engineering, Seoul National University, Seoul, South Korea, in 2001 and 2008, respectively. In 2008, he was with the School of Mechanical and Aerospace Engineering, Seoul National University, where he was a Postdoctoral Fellow. Since 2010, he has been with the Korea Institute of Science and Technology (KIST). In KIST, he was a Senior Researcher, from 2010 to 2016, and he has been a Principal Researcher, since 2016. His areas of interests are indoor navigation systems, pattern recognition, and sensor networks.

CHANGDON KEE received B.S. and M.S. degrees from Seoul National University, and the Ph.D. degree from Stanford University.

He is currently a Professor with the School of Mechanical and Aerospace Engineering, Seoul National University (SNU), South Korea, and supervises SNU GNSS Lab (SNUGL). He has served as a Technical Advisor to the Federal Aviation Administration (FAA) on the Wide Area Augmentation System (WAAS), in 1994. Prof. Kee serves as a Technical Advisor for the Korea Civil Aviation Safety Authority (KCASA) and Ministry of Public Administration and Security (MOPAS). He also served as the President of the Korean Institute of Navigation. He has more than 20 years of GNSS and flight control research experience.